Brain Stimulation 15 (2022) 1236–1245

Contents lists available at ScienceDirect

Brain Stimulation

journal homepage: http://www.journals.elsevier.com/brain-stimulation

Transcranial ultrasound stimulation to human middle temporal complex improves visual motion detection and modulates electrophysiological responses

Christopher R. Butler [a, b, *, 1], Edward Rhodes [a, c, 1], Joseph Blackmore [d], Xinghao Cheng [d], Robert L. Peach [a, e], Michele Veldsman [f], Fintan Sheerin [g], Robin O. Cleveland [d]

[a] Department of Brain Sciences, Imperial College London, UK
[b] Nuffield Department of Clinical Neurosciences, University of Oxford, UK
[c] UK Dementia Research Institute, Imperial College London, UK
[d] Institute of Biomedical Engineering, University of Oxford, UK
[e] Department of Neurology, University Hospital of Würzburg, Germany
[f] Department of Experimental Psychology, University of Oxford, UK
[g] Oxford University Hospitals NHS Foundation Trust, Oxford, UK

ARTICLE INFO

Article history:
Received 24 January 2022
Received in revised form
29 August 2022
Accepted 30 August 2022
Available online 5 September 2022

ABSTRACT

Background: Transcranial ultrasound stimulation (TUS) holds promise as a novel technology for non-invasive neuromodulation, with greater spatial precision than other available methods and the ability to target deep brain structures. However, its safety and efficacy for behavioural and electrophysiological modulation remains controversial and it is not yet clear whether it can be used to manipulate the neural mechanisms supporting higher cognitive function in humans. Moreover, concerns have been raised about a potential TUS-induced auditory confound.

Objectives: We aimed to investigate whether TUS can be used to modulate higher-order visual function in humans in an anatomically-specific way whilst controlling for auditory confounds.

Methods: We used participant-specific skull maps, functional localisation of brain targets, acoustic modelling and neuronavigation to guide TUS delivery to human visual motion processing cortex (hMT+) whilst participants performed a visual motion detection task. We compared the effects of hMT+ stimulation with sham and control site stimulation and examined EEG data for modulation of task-specific event-related potentials. An auditory mask was applied which prevented participants from distinguishing between stimulation and sham trials.

Results: Compared with sham and control site stimulation, TUS to hMT+ improved accuracy and reduced response times of visual motion detection. TUS also led to modulation of the task-specific event-related EEG potential. The amplitude of this modulation correlated with the performance benefit induced by TUS. No pathological changes were observed comparing structural MRI obtained before and after stimulation.

Conclusions: The results demonstrate for the first time the precision, efficacy and safety of TUS for stimulation of higher-order cortex and cognitive function in humans whilst controlling for auditory confounds.

© 2022 Published by Elsevier Inc. This is an open access article under the CC BY-NC-ND license (http://creativecommons.org/licenses/by-nc-nd/4.0/).

1. Introduction

Non-invasive brain stimulation (NIBS) provides a means for causal inference when investigating brain-behaviour relations as well as having potential therapeutic applications. However, current NIBS methods, such as transcranial magnetic stimulation (TMS) and transcranial electrical stimulation (TES), have poor spatial

* Corresponding author. Department of Brain Sciences, Imperial College London, UK.
E-mail address: christopher.butler@imperial.ac.uk (C.R. Butler).
[1] These authors contributed equally to the work.

https://doi.org/10.1016/j.brs.2022.08.022
1935-861X/© 2022 Published by Elsevier Inc. This is an open access article under the CC BY-NC-ND license (http://creativecommons.org/licenses/by-nc-nd/4.0/).

resolution and are limited to targeting relatively superficial cortical regions. Transcranial ultrasound stimulation (TUS) is an emerging technology for reversible NIBS which offers unprecedentedly high spatial and temporal resolution and the ability selectively to target deep brain structures [1]. The mechanisms by which TUS exerts its effect on neurons are not yet fully understood but are thought to involve interactions between acoustic radiation forces and mechanosensitive ion channels [1]. In animal models, TUS can induce focal motor responses [2]; alter functional magnetic resonance imaging (fMRI) blood oxygen level-dependent (BOLD) responses [3] and electroencephalography (EEG) signals [4]; and, in non-human primates, cause changes in behavioural performance on complex cognitive tasks [5]. A small number of studies in humans have reported neuromodulatory effects of TUS in primary sensory [6–9] and motor [10–14] cortex and the thalamus [15,16]. No study has yet determined whether TUS is able to modulate human higher cognitive processes and their neural substrates in a spatially and temporally specific manner. Such evidence would be a crucial step towards widespread application of TUS in cognitive neuroscience and towards clinical utility of the technique.

However, the validity of previous experimental results has recently been called into question by the demonstration of TUS-induced auditory stimulation that introduces both behavioural and neurophysiological confounds [17–20]. The auditory effect is likely due to direct cochlear activation by skull conducted shear waves at the ultrasound pulse repetition frequency (PRF) [19,21], but may be mitigated by simultaneous presentation through earphones of a frequency-matched masking sound on both stimulation and sham trials [19]. Controlling for such confounds is critical to ensure that measured behavioural or physiological effects are indeed due to direct neural modulation by TUS.

There are various technical challenges involved in accurately focusing TUS in the human brain, particularly due to individual variability in skull geometry, tissue properties and the precise location of the target region. To date, this variability has rarely been considered in pre-stimulation planning for neuromodulation, despite its potential to critically influence the safety and efficacy of the acoustic field [22].

We investigated whether TUS can be used to manipulate higher-order perceptual function and its electrophysiological correlates in an anatomically specific way. We stimulated the human middle temporal complex (hMT+, also known as V5), a small region of extra-striate cortex highly selective for visual motion processing [23], whilst participants made judgements about the average direction of movement of random-dot kinetograms. We compared hMT+ stimulation to that of a control site (the fusiform face area, FFA), also involved in higher order visual processing, but of faces rather than motion [24]. Any acoustic confound associated with TUS was removed with auditory masking. EEG data were collected to probe the underlying neural responses to stimulation. Ultrasound transducer placement was determined using a participant-specific pre-stimulation pipeline for each brain target and the safety of TUS was addressed by modelling of transcranial acoustic and thermal fields. Safety was evaluated by pre- and post-stimulation neuroimaging.

2. Methods

2.1. Participants

16 participants (10 females, 6 males) took part in the experiment (mean age: 26; range 20–51). All gave written consent and were given an honorarium for participating, in compliance with procedures approved by the University of Oxford Medical Sciences Interdivisional Research Ethics Committee. All had normal vision and reported that they were in good health with no history of neurological disease.

2.2. Magnetic resonance imaging

All participants underwent pre-stimulation head MRI for planning of the ultrasound stimulation. A subset of 13 participants also underwent post-stimulation MRI for safety monitoring purposes. Scanning was performed at the Oxford Centre for Clinical Magnetic Resonance Research using a 3 T Siemens Trio scanner equipped with a 32-channel head coil. High-resolution T1-weighted images were acquired using a three-dimensional magnetisation-prepared rapid-acquisition gradient-echo pulse sequence (repetition time (TR), 3000 ms; echo time (TE), 4.71 ms; flip angle, 8°; voxel size, 1 × 1 × 1 mm; field of view, 192 mm). T2-weighted (TR, 3390 ms; TE, 390 ms; voxel size, 1 × 1 × 1 mm; field of view, 256 mm) and susceptibility-weighted imaging (SWI; TR, 27 ms; TE, 20 ms; flip angle, 15°; voxel size, 0.9 × 0.9 × 1.5 mm; field of view, 220 mm), sensitive to extravasated blood products, was also performed in order to detect any microbleeds or other pathology induced by TUS.

In order to localise the ultrasound target and control sites, T2*-weighted images sensitive to blood oxygenation level-dependent contrast were acquired using a gradient-echo echoplanar pulse sequence (TR, 2410 ms; TE, 30 ms; flip angle, 90°; voxel size, 3 × 3 × 3 mm; field of view, 192°; matrix size, 64 × 64 × 44; multiband acceleration factor of 2). Ten additional fMRI volumes, which were excluded from data analysis, were also collected at the start of each scan run to account for signal steady-state transition.

Visual stimuli were displayed at the rear bore face on a flat panel screen. Participants viewed the screen via a mirror attached to the head coil. Behavioural responses were collected using a fibre-optic button box.

Standard, block-design procedures were used to localise hMT+ [25] and the control site (the fusiform face area, FFA) [26]. Briefly, for localisation of hMT+, participants viewed patches of centrally-presented moving or static dots in 20 blocks (10 moving blocks, 10 static blocks, in a pseudorandomised order) of 15 trials per block. Participants responded with a button press according to the colour (yellow or blue) of a filled circle at the centre of the dot patch. For localisation of FFA, participants viewed centrally-presented images of faces or houses in 20 blocks (10 face blocks, 10 house blocks, in a pseudorandomised order) of 15 trials per block. Participants performed a 1-back task, responding with a button press according to whether the current stimulus was the same as or different from the immediately preceding stimulus.

MRI preprocessing and analysis were performed using Statistical Parametric Mapping software (SPM12; fil.ion.ucl.ac.uk/spm/software/spm12) in Matlab R2019b. Segmentation of T1-weighted scans was carried out to assign each voxel to one of five tissue types: scalp tissue, skull bone, cerebrospinal fluid (CSF), white and grey matter. Segmentations were manually inspected for quality assurance. The fMRI data preprocessing pipeline comprised motion correction, slice-time correction, coregistration to the participant's structural image and smoothing with an 8 mm FWHM Gaussian kernel. A high pass filter with a cut-off of 128 s was applied to remove low-frequency noise. The regressors of interest for the hMT+ localiser were motion vs static trials. The regressors of interest for the FFA localiser were faces vs houses trials. Events were convolved with the canonical hemodynamic response function and a general linear model (GLM) was fitted voxel-wise. The right hemisphere maximum in the ascending branch of the inferior occipital sulcus for moving vs static dots was used as the centre of a 5 mm spherical target for hMT+. The right hemisphere maximum within the fusiform gyrus for faces vs houses was used as the centre of a 5 mm spherical target for FFA.

Pre- and post-stimulation raw structural images (T1, T2, SWI) were checked and compared by a consultant neuroradiologist (FS) to identify any differences potentially attributable to TUS.

2.3. Ultrasound targeting protocol

To determine the appropriate position and driving voltage of the US transducer in order to sonicate hMT+, participants underwent a US targeting modelling pipeline based on the T1-weighted images (Fig. 1a). This structural information informed the property maps for US wave propagation simulations in k-Wave, an open-source, k-space, pseudospectral, time-domain solver [27,28]. The skull was assumed to be an effective fluid (i.e. shear waves were neglected which was justified by the near-normal incidence of the ultrasound) and nonlinear phenomena were ignored (which was justified by the pressure amplitude of the ultrasound). Acoustic properties for each tissue type were assigned according to Table 1. Coupling of the source to the scalp was assumed to be perfect with the head modelled as being immersed in water although hydrophone coupling experiments indicated that, in reality, a minimum of a 10% pressure loss was likely [29].

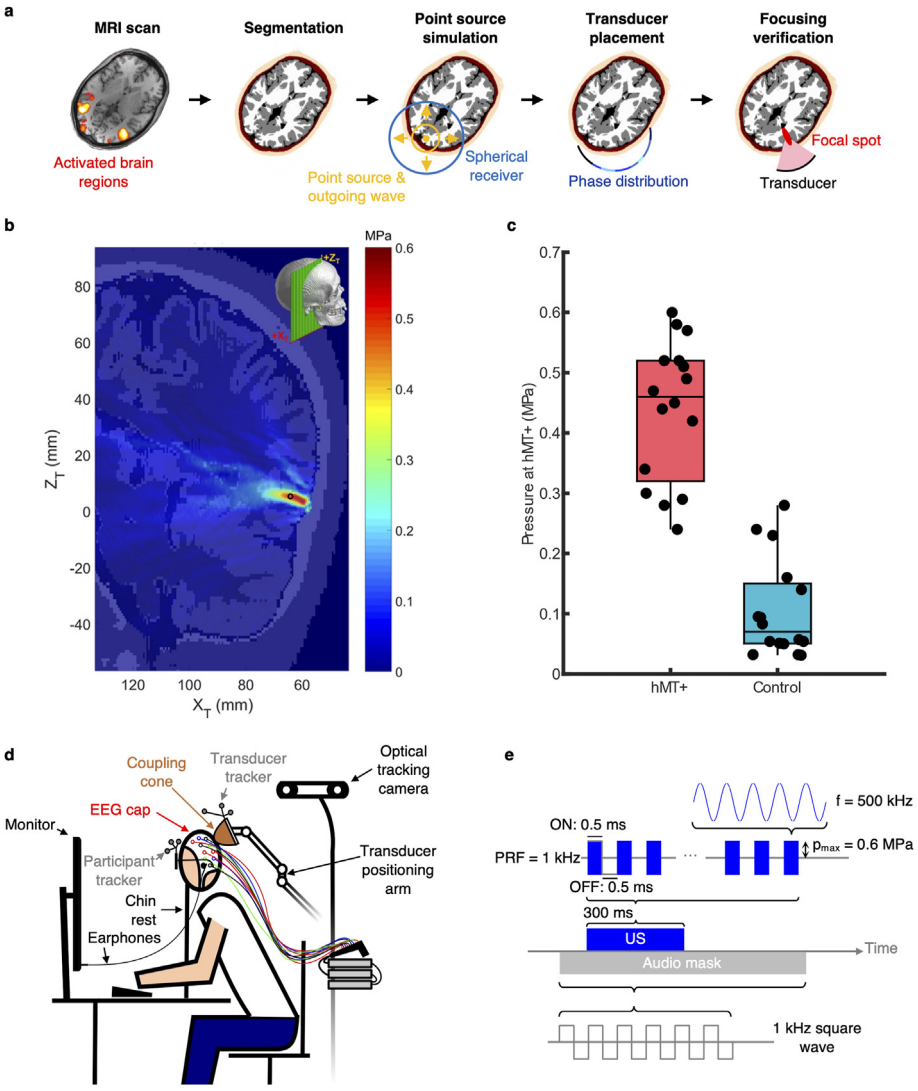


Fig. 1. | TUS experimental setup and methodology overview. **a**, Summary of US modelling pipeline. Structural and functional MRI scans informed participant-specific tissue segmentation and hMT+/control site localisation. A numerical point source was propagated transcranially from this site to a spherical receiver corresponding to a sphere with radius equal to the focal length of the transducer. Visual inspection of the phase field over the surface determined transducer placement to refocus to the target which was verified by forward simulations. **b,** Representative simulated US field for a representative participant targeting hMT+ overlaid onto the segmented tissue map through an on-axis vertical plane relative to the US transducer; orientation relative to the skull is shown in the top right-hand corner. The black circular marker indicates the target (hMT+). In simulation space, each voxel has its tissue type specified by a coding system. Only the US field in CSF and brain is kept visible here. The US field in other tissues is set to 0 for clarity. For additional pressure field maps for targeting hMT+ and the control site see Supplementary Figs. 2a and 2b **c,** Modelled target pressures at hMT+ when targeting hMT+ and control site for all participants. **d,** Schematic of the experimental setup: a 64-electrode EEG cap, with a cut-out over the posterior right hemisphere for US transducer coupling, was fitted to the head. Transducer positioning was guided by the Brainsight neuronavigational system which utilised an optical tracking camera, and adjusted through a custom-built arm. The position was manually updated throughout all tasks to ensure correct alignment as informed by the Brainsight system which tracked the position of the participant's head and the transducer through reflective silver optical trackers. Coupling of the transducer to the scalp was achieved using a polyurethane membrane expanded through the addition of degassed water to adjust its depth, and US gel. A set of earphones played an audio masking tone mimicking the US burst sequence. **e,** Each TUS trial comprised of 0.5 ms pulses of 500 kHz US at a 1 kHz PRF (50% duty cycle) with a 300 ms burst length. The amplitude was adjusted to deliver a modelled peak positive pressure at the target as close to 0.6 MPa as possible, without exceeding that value elsewhere in the brain or CSF. The audio mask was a 1 kHz square wave that started approximately 110 ms before TUS onset and lasted 700 ms.

Table 1
Acoustic and thermal tissue properties.

Material	Density [kg/m^3]	Sound speed [m/s]	Attenuation [dB/cm]	Thermal conductivity [W/(mK)]	Specific heat capacity [J/(kgK)]
Water [30]	1000	1488	0	0.6	4178
Scalp [31,32]	1000	1500	0.15	0.528	3600
Skull [30,33]	1732	2820	3.28	0.32	1313
CSF [30]	1007	1504.5	0.004	0.57	4096
White matter [30]	1041	1552.5	0.29	0.48	3583
Grey matter [30]	1045	1500	0.05	0.55	3696

Simulations were carried out at a grid spacing of 0.5 mm, equating to 5.95 points per wavelength in water in keeping with previous k-Wave modelling studies [34,35]. The Courant-Friedrichs-Lewy number was set at 0.3 for all simulations. The domain size of 140.4 mm (300 points per dimension plus a 10 point absorbing perfectly-matched layer) did not include the opposite skull wall which was deemed satisfactory based on preliminary simulations where standing wave effects were found to be negligible [29]. By restricting the domain size, simulations could be carried out in ~240 s using an NVIDIA Titan Xp GPU with 12 GB of onboard RAM.

In order to determine the best positions of the ultrasound transducer to insonify the targets and minimise beam distortion as a result of the presence of the skull, a computational treatment planning process was employed. First, a numerical point source was located at the desired target (hMT+ or the control site, FFA) and ultrasound waves at 500 kHz were propagated out through the skull to a spherical surface corresponding to a sphere with radius equal to the focal length of the transducer. Simulations were run for 100 US cycles to determine the steady-state pressure distribution, accounting for any wave interactions from the closest skull surface. Because the wave equation obeys reciprocity, the recorded signals on this surface can be used to determine the source conditions needed to refocus to the target. The phase and amplitude were extracted by means of a discrete Fourier Transform at each grid point and then interpolated onto the exact spherical surface to mitigate finite grid spacing staircasing errors. In the second step, visual inspection of the field on the spherical surface was used to identify regions of more uniform phase, which were then used to manually select potential candidate locations for the source transducer. For each candidate location, a forward simulation was computed for the actual source: the source condition was determined by acoustic holography of the H-107 transducer where a measured plane is back-propagated to the source plane [29,36]. From the forward simulations, the transcranial, in situ pressure fields were used to assess the focal spot size and target amplitude for each candidate location. The optimal transducer location was then chosen for that participant. This process was done for both hMT+ and the control site.

Thermal simulations were also performed using the k-Wave toolbox. The simulations solved the Pennes bio-heat transfer equation [37], whereby the input heating rate was calculated from the acoustic field by assuming a local plane wave [38]. Test simulations were used to determine that a timestep of 300 ms, matching the length of the applied US burst, led to a stable numerical solution [29]. Tissue-specific thermal properties were assigned as given in Table 1, and blood perfusion properties were defined as: blood perfusion rate, $w = 0.08/s$; blood density, $\rho_b = 1030$ kg/m^3; blood specific heat capacity, $c_{p,b} = 3620$ J/(kgK); and arterial temperature, $T_a = 37$ °C. Simulations were run for a total of 200 ultrasound stimulation trials at an inter-stimulation interval of 2.4 s (Supplementary Fig. 1). During the behavioural experiment, actual ISIs (cooling period) ranged between 3 s and 5.4 s for stimulation trials and there were randomly interleaved sham trials. The predicted thermal fields were therefore expected to be overestimated. The pressure amplitude of the ultrasound was then set to ensure the modelled pressure and temperature fields satisfied safety criteria. The following safety criteria, concordant with FDA guidelines [31] and previous human TUS studies [22], were set: i) maximum peak pressure in brain or CSF of 0.6 MPa; ii) spatial peak, temporal averaged intensity (I_{SPTA}) < 720 mW/cm^2; iii) maximum of 250 ultrasound stimulation bursts per brain site; iv) temperature rise <3 °C in skull bone and; v) temperature rise <1 °C in brain tissue. Modelling predicted a group mean pressure at hMT+ of 0.44 ± 0.12 MPa during hMT+ stimulation and 0.11 ± 0.08 MPa during control site stimulation (Fig. 1b and c, Supplementary Table 1, Supplementary Figs. 2a and 2b).

2.4. Ultrasound stimulation

Sonications were performed using a 500 kHz single-element geometrically-focused (64 mm aperture, 63.1 mm radius of curvature) US transducer (H-107, Sonic Concepts Inc, Bothell, WA, USA). Focal pressure calibration of the transducer was completed using a needle hydrophone (model HNA-400, ONDA, Sunnydale, CA, USA) up to a peak output amplifier voltage of 100V which corresponded to a maximum peak positive freefield pressure of ~3.5 MPa. Ten repeat measurements were taken at each voltage step and the results were highly repeatable. In the range of amplifier voltages used in this study (up to 60V), the relationship between amplifier voltage and peak pressure was linear (Supplementary Figs. 3a and 3b).

A stimulation trial comprised a 300 ms burst applied at a 1 kHz pulse repetition frequency (PRF) and a 50% burst duty cycle (BDC) (Fig. 1e). The stimulation waveform was generated from an arbitrary waveform generator (Handyscope HS5, TiePie, WL Sneek, The Netherlands), amplified by a 55 dB broadband amplifier (1140LA, E&I, Rochester, NY, USA), and connected to the transducer via a matching network. The voltage waveform applied to the transducer was measured by the digital oscilloscope channel of the HS5 and as a safety check if the amplitude exceeded the specified voltage by more than 10% the trial was halted, which did not happen in practice. Synchronicity between the US system and arbitrary waveform generator was achieved by sending a timing pulse from the waveform generator to a spare EEG channel.

Coupling of the US transducer to the scalp was accomplished via the use of a flexible polyurethane membrane secured around the edges of the transducer using a custom mount. Degassed water was injected into the cavity through syringe connections located on a backplate over the transducer's central circular cut-out. The external membrane surface was coupled to the participant's scalp via liberal application of US coupling gel (Parker Aqua Sonics 100). The participant's hair was not shaved for the experiment [39] and the gel was gently massaged into the hair in order to reduce air voids. Transducer placement was informed by a neuronavigation system (Brainsight; Rogue Resolutions; https://www.rogue-resolutions.com) which utilised optical trackers on both the transducer and the participant (attached via a set of clear-lens

glasses) (Fig. 1d, Supplementary Fig. 4). Targeting accuracy was monitored on a trial-by-trial basis for 9/16 participants. The overall mean error was 1.09 ± 0.85 mm (Supplementary Table 2).

2.5. Auditory masking

Auditory masking signals were played through earphones, inserted into the auditory canal, that were driven by the earphone jack on the computer. The masking signal was a 1 kHz square wave with a duration of 700 ms which was created in Matlab 2019b and used the in-built playsound function. The amplitude of the masking signal was determined prior to the main behavioural experiment, by means of a stimulation detection task for each stimulation site (hMT+ and the control site) for each participant. During this task, 40 trials (20 stimulation, 20 sham) were presented in randomised order. Participants were asked to keep their eyes fixed on a cross at the centre of the computer screen. They were told that stimulation might lead to a detectable sound, a feeling on the skin or some other sensation. They were asked to respond by pressing one of two keys on a keyboard on each trial according to whether they thought it was a stimulation or sham trial. In stimulation trials, TUS was applied to the target site 2.7–3 s after fixation onset for 300 ms before a question mark appeared prompting participants to indicate whether they thought they were stimulated or not. In sham trials, no TUS was delivered; in stimulation trials, the 300 ms long US burst was applied 112 ms after the onset of the mask (due to the latency in the Matlab scripts) (Fig. 1e). If the participant reported being able to detect a difference between stimulation and sham trials, the stimulation detection task was repeated with the tone played at an increased volume. The mask volume needed to be increased for 4 of the 16 participants. No discomfort was reported by any of the participants as a result of the auditory masking.

2.6. Behavioural task

To assess potential behavioural effects of hMT+ stimulation, we used a visual motion coherence detection task (Fig. 2a and b).

2.6.1. Stimuli

Stimuli consisted of a 10° × 10° random-dot kinetogram (RDK) of white dots on a black background displayed at 10° to the right or left of fixation. A proportion of the dots moved coherently at 120°/second either to the left or the right, whilst the remainder moved randomly. The difficulty of the trial was controlled by changing the proportion of dots displaying coherent motion. Stimuli consisting of an array of static dots were also designed for use as catch trials, to ensure that participants were engaged in the task, and as a comparator for motion trials in the EEG analyses.

2.6.2. Experimental setup

Participants were seated, with a chin rest to minimise head movement and the eyes at 50 cm from the computer screen on which the visual stimuli were displayed (at which distance 10° corresponded to 8.8 cm). Responses were made with the right hand on a computer keyboard. Participants wore earphones in both ears throughout the experiment. The behavioural task was implemented using PsychToolbox (v3.0, http://psychtoolbox.org) running in Matlab 2019b. Participants were instructed to maintain their gaze at a fixation cross at the centre of the screen.

2.6.3. Task structure

Approximately 112 ms before the onset of each trial, an audio signal was played to the participant through earphones to mask any auditory confound of TUS. At the onset of each trial, the stimulus was displayed for 300 ms, during which time TUS was either delivered (stimulation trials) or not (sham trials) to the target (hMT+) or the control (FFA) site. Following the offset of the stimulus, there was a randomly jittered fixation period of 800–1200 ms to avoid motor-related EEG changes during the stimulation period. This was followed by a response period of 1500 ms, signalled by the fixation cross changing to a small blue circle. The participant was instructed to respond as soon as the blue dot appeared, indicating which direction the dots were moving in. The direction decision was indicated on the computer keyboard, using the right hand to depress the left or right arrow key with the first and second finger

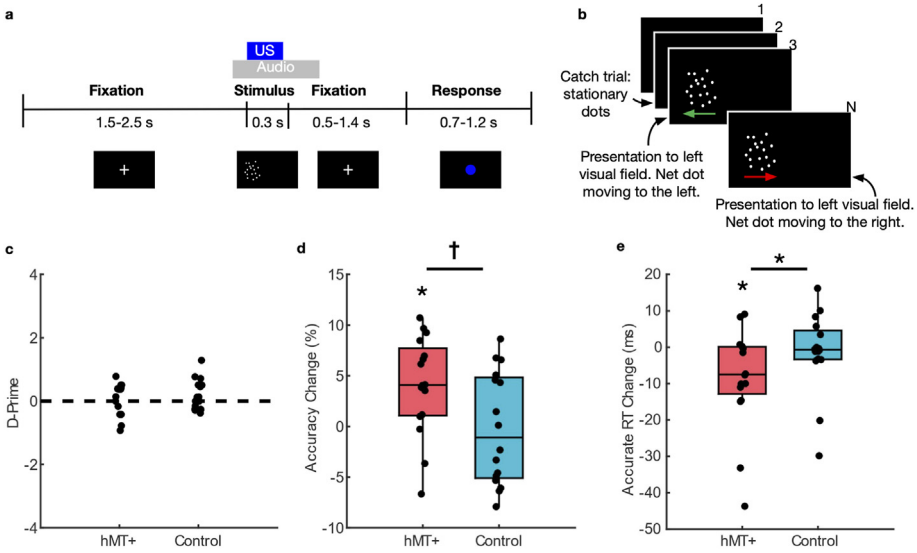


Fig. 2. | Behavioural task and results **a**, Trial structure of the behavioural task. **b**, Random Dot Kinetogram stimuli used in the behavioural task. **c,** D-prime values from the stimulation detection task show that participants were unable to detect stimulation with either hMT+ or control site stimulation. **d**, hMT+ stimulation resulted in a significant improvement in motion detection accuracy. Stimulation of the control site had no effect. There was a significant interaction between stimulation site and condition. **e**, hMT+ stimulation also significantly improved participant response times during accurate responses ($p = 0.027$) while control site stimulation had no significant effects. *$p < 0.05$; †$p < 0.050$.

respectively. Participants were instructed to press the 'up' arrow for static trials.

The task began with a 'practice' session in which participants viewed 20 trials in each hemifield (order of hemifield presentation randomised) with a fixed proportion of 70% coherent motion. After each trial in the practice session, the participant received feedback as to whether their response was correct or incorrect. If the participant scored <80% correct, the practice block was repeated.

When the practice session had been completed with >80% correct responses, the experiment moved immediately to the 'titration' session which determined the mean and standard deviation motion coherence at which the participant gave an accurate response on 70% of trials. This procedure utilised the QUEST procedure [40] implemented in PsychToolbox. The threshold was determined over 50 trials for each hemifield, with randomised order of hemifield presentation. The trial structure was identical to the practice session except that no feedback was provided to the participant.

The main experiment was divided into three runs each of 90 trials. For each trial, motion coherence was randomised to be at the mean, ±0.25 SD or ±0.50 SD of the 70% accuracy threshold determined for that hemifield in the preceding 'threshold' run. This variability was kept tight around the threshold due to pilot work suggesting that the TUS effect was not detectable if the trial was too easy or too difficult. The total number of trials that could be delivered to each participant was limited by our safety constraints (see Ultrasound Targeting Protocol above). 10 trials in each run (30 in total) were static trials. Otherwise, the trial procedure was identical to the 'threshold' session. The main experiment was run twice, once with TUS targeted at hMT+ and once with it targeted at FFA, the order being counterbalanced across participants.

2.7. Behavioural data analysis

Our behavioural measures of interest were accuracy (the proportion of all trials in which the participant's response correctly indicated the direction of coherent motion in the visual stimulus) and response time (RT) (the time difference in milliseconds between the onset of the response cue and the participant's response. Repeated measures ANOVAs were used to analyse the behavioural results and included factors of stimulation (ON, OFF), target (hMT+, control FFA), accuracy (CORRECT, INCORRECT), direction of response (LEFT, RIGHT) and hemifield (LEFT, RIGHT). Correlational analyses were used to investigate relationships between behavioural measures across participants and i) mean ultrasound pressure at the target and ii) mean amplitude of the ERP waveform. In order to assess any effect of time on task, we averaged behavioural results across bins of 30 consecutive motion trials and conducted repeated-measures ANOVAs to detect any interaction between bin number and the effect of stimulation versus sham on behaviour.

To assess whether participants' ability to detect TUS had any effect on our behavioural outcomes, Bayes Factor analysis was performed contrasting d-prime detection values with TUS to hMT+ induced changes in accuracy and response times. Bayesian t-tests were also performed to determine whether participants were able to detect TUS trials at greater than chance levels. All Bayesian statistics were calculated using JASP (version 0.15; JASP Team, 2021).

2.8. Electroencephalography

2.8.1. EEG acquisition and preprocessing

EEG was recorded from 52 Ag/AgCl sintered ring electrodes (BrainProducts 64-channel BrainAmp DC, BrainProducts GmbH, Gilching, Germany) arranged according to the 10%-system at a sampling rate of 500 Hz (low cutoff 10 s, high cutoff 250 Hz) referenced to FCz. EEG data were preprocessed and analysed using the Fieldtrip toolbox [41] in Matlab 2019b, as well as with custom-made Matlab scripts. Continuous EEG data were subdivided into 240 trials per participants, with each trial beginning 1000 ms before stimulation onset and ending 1500 ms after stimulation onset. Long trial duration was used to prevent edge artefacts being introduced by filtering and frequency analysis. Blink artefacts were found using the EOG channel along with the FP1 and FP2 channels. Any deflection greater than 4SD from the trial mean was considered to be a blink or saccade. Any trial that contained a blink was rejected. Given the absence of EEG channels underneath the transducer, data were not re-referenced to an average reference but rather to a central reference. Trials were bandpass filtered between 1 and 30Hz using a Butterworth, 2nd order, two-pass filter. Line noise at 50Hz was also removed using a discrete Fourier transform estimation. Trials were normalised to a baseline window from −215 ms to −115 ms in relation to TUS onset (i.e. prior to the onset of the audio mask). Finally, trials were subdivided into conditions, stimulation and sham.

2.8.2. EEG analysis

Data from an initial pilot study were used to identify channels that demonstrate a motion-specific ERP. This additional, independent dataset allowed for the identification of channel clusters that are significantly different during motion detection than when observing static dots without biasing any further analysis performed on the current dataset by double-dipping.

The pilot study was performed on 19 participants (8 male, mean age: 26; range: 20–46), and consisted of the same visual motion coherence detection task described above, with some key differences. There were a greater number of trials during the pilot, 450 in total, consisting of 50 static trials and 400 motion trials, of which 200 were also stimulation trials. The modulation of task difficulty also differed as motion coherence was randomised to be at the mean, ±2 SD or ±4 SD of the 70% accuracy threshold determined for that hemifield. Finally, there was no TUS control site target during the pilot, with all stimulation targeted at hMT+.

To assess differences between ERPs two main contrasts were made using a cluster-based permutation test: ERPs generated during sham static trials were compared with sham motion trials from the initial pilot study and, from the present study, motion ERPs generated during hMT+ stimulation were compared with sham trials.

Cluster-based permutation testing consists of two parts: first, uncorrected dependent samples paired t-tests (two-tailed) were performed and all channels and/or time-points that surpassed a 2.5% significance threshold were grouped into clusters. Channel clusters were aggregated based on the distance between electrodes, calculated by triangulating the 2D layout of the cap used. Time-point clusters were aggregated based on neighbouring samples that fell within the stimulation window (0–300 ms). The sum of t-values within each cluster was then compared to a null distribution. The null distribution was generated by randomly permuting condition label 524,2800 or 65,576 times (2^(number of participants) in the pilot and present study respectively) and calculating the maximum cluster t-value sum for each permutation. The maximum t-sum for each original cluster was then contrasted with the null distribution and significant ($p < 0.025$) clusters were extracted.

Similarly, ERP amplitude was correlated with behavioural performance using a cluster-based permutation approach whereby the correlation coefficient between the amplitude at each timepoint and accuracy change was computed. Permutations were then used to randomise participant labels and timepoints to generate the null

distribution. Original clusters that were significantly larger than the null distribution (threshold of 2.5%) were extracted.

3. Results

3.1. Successful masking of TUS-induced auditory signal

To mask the potential auditory confound of TUS, an audio signal that was identical to the modulation envelope of the ultrasound (i.e., 1 kHz square wave), was played to participants through earphones on all trials (Fig. 1e). In the stimulation detection task, conducted immediately before the main behavioural experiment, participants reported no auditory signal difference between TUS and sham stimulation (no ultrasound delivered, acoustic mask only) trials. No participant reported visual effects of TUS such as phosphene perception. One-sample Bayesian t-tests supported the hypothesis that participants were unable to distinguish between TUS and sham stimulation trials: i.e. the signal detection metric (d-prime) was not different from zero with the transducer targeting hMT+ (d-prime: mean = 0.098 ± 0.501; ($C(0,1/\sqrt{2})$, $BF_{01} = 2.994$, median = 0.135, 95% credible interval (CI) = [−0.143, 0.810]) or the control site (d-prime: mean = 0.181 ± 0.480; ($C(0,1/\sqrt{2})$, $BF_{01} = 1.520$, median = 0.321, 95% CI = [−0.284, 0.630]) (Fig. 2c). Furthermore, a paired *t*-test supported the hypothesis that there was no difference in ability to detect stimulation from sham trials at hMT+ and the control site ($C(0,1/\sqrt{2})$, $BF_1 = 3.546$, median = 0.100, 95% CI = [−0.347, 0.557]).

3.2. TUS to hMT+ improves visual motion detection

In the visual motion detection experiment, participants viewed random-dot kinetograms in the left or right visual hemifield and judged the average direction of movement of the dots (left or right). Interleaved arrays of static dots, with sham stimulation only, were used as catch trials and for an EEG comparator condition. TUS and sham stimulation trials were interleaved in a pseudorandomised order (Fig. 2a and b). hMT+ and the control site were stimulated in separate experimental blocks, counterbalanced for order across participants. Due to practical constraints of the ultrasound set-up, only the right hemisphere targets were stimulated. We predicted that stimulation effects would not lateralise: whilst some hMT+ neurones show hemifield specific responses, others have large receptive fields that cross the midline [42] and TMS affects motion perception in both the contralateral and ipsilateral visual hemifield [43]. In sham stimulation trials, participants performed close to the intended 70% accuracy (mean = 67.5% ± 6.7). Crucially, a 2 × 2 repeated measures ANOVA (stimulation (ON, OFF), target (hMT+, control site)) for accuracy revealed an interaction of stimulation with target ($F(1,15) = 4.688$, $p = 0.047$, $\eta_p^2 = 0.238$). Accuracy improved with TUS vs sham to hMT+ ($t(15) = 3.350$, $p = 0.004$, $d = 0.838$) but not with TUS vs sham to the control site ($t(15) = -0.144$, $p = 0.887$, $d = 0.036$) (Fig. 2d). We also examined TUS effects on reaction times for both accurate and inaccurate trials, since a motion perception advantage driven by hMT+ stimulation might affect these differentially [44]. A 2 × 2 × 2 repeated measures ANOVA (stimulation (ON, OFF), target (hMT+, control site), accuracy (CORRECT, INCORRECT)) for reaction time revealed a significant interaction effect between stimulation, target and accuracy ($F(1,15) = 5.717$, $p = 0.030$, $\eta_p^2 = 0.276$). For accurate trials, reaction time decreased with TUS compared with sham to hMT+ ($t(15) = -2.448$, $p = 0.027$, $d = 0.612$) but not with TUS to the control site ($t(15) = -0.466$, $p = 0.648$, $d = 0.117$) (Fig. 2e). For inaccurate trials, reaction time increased with TUS to hMT+ ($t(15) = 2.378$, $p = 0.031$, $d = 0.594$) but not with TUS to the control site ($t(15) = -1.008$, $p = 0.330$, $d = 0.252$). These results demonstrate a beneficial effect of hMT+ TUS, compared with control site stimulation and sham, on both the accuracy and speed of visual motion perception judgements.

There was no significant correlation across participants between behavioural performance changes with TUS to hMT+ and performance (d-prime) on the stimulation detection task either for accuracy ($r\ [2] = 0.175$, $p = 0.107$) or reaction time ($r\ [2] = 0.128$, $p = 0.174$). The effect of TUS to hMT+ did not change over the course of the experiment either for accuracy ($F(8,120) = 1.410$, $p = 0.199$, $\eta_p^2 = 0.086$) or reaction time ($F(8,120) = 1.320$, $p = 0.238$, $\eta_p^2 = 0.081$), suggesting that the behavioural effects of TUS in this protocol were short-lived and non-cumulative. The effect of TUS also did not depend upon the modelled pressure at hMT+ across participants either for accuracy ($F(1,14) = 0.584$, $p = 0.458$, $r^2 = 0.040$) or reaction time ($F(1,14) = 0.365$, $p = 0.555$, $r^2 = 0.025$) (Supplementary Figs. 5a and 5b). As expected, the behavioural effect of TUS to hMT+ did not depend on the hemifield to which the dots were presented, either for accuracy ($F(1,15) = 1.665$, $p = 0.216$, $\eta_p^2 = 0.100$) or reaction time ($F(1,15) = 0.003$, $p = 0.957$, $\eta_p^2 = <0.001$). Furthermore, a 2 × 2 repeated measures ANOVA (stimulation (ON, OFF), target (hMT+, control site)) for direction of response (LEFT, RIGHT) revealed that TUS did not bias participants towards either 'left' or 'right' responses ($F(1,15) = 1.741$, $p = 0.207$, $\eta_p^2 = 0.104$).

3.3. TUS modulates the visual motion evoked ERP

Previous work has revealed a now well-characterised ERP to visual motion comprising an early positive deflection at around 130 ms (P1), a subsequent negative deflection at around 160–200 ms (N2), then a further positive deflection with more variable onset after about 240 ms (P2) [45]. To investigate the electrophysiological effects of TUS, we first analysed data collected during an earlier pilot study (see Methods) to identify a cluster of 16 EEG channels that showed a motion-specific ERP (Fig. 3a inset, Supplementary Fig. 6). Averaging across this cluster in our main experiment, the ERP for motion and static trials differed in three time windows: 68–88 ms, 110–174 ms and 254–272 ms (Fig. 3a). We note that the use of an auditory mask in our experiments (which began approximately 110 ms prior to the presentation of the visual stimulus) produced an auditory ERP that will have altered the subsequent visual motion evoked response (Fig. 3a–c) [19]. With the further cautionary note that the removal of electrodes to allow for transducer placement may also have affected observable ERP responses, we next examined the effect of TUS to hMT+ compared with sham in the identified channel cluster. Applying cluster-based permutation tests, we found that TUS caused a significant reduction in ERP amplitude between 236 and 260 ms (Fig. 3b), a time window overlapping with the third visual motion specific ERP component. In order to detect target-specific electrophysiological effects of TUS, we next compared the ERP during trials with stimulation to hMT+ and the control site, and found a significant difference in amplitude between 114 and 154 ms (Fig. 3c), a time window overlapping with the second visual motion specific ERP component. The fact that there were distinct time windows for the differences between hMT+ and sham versus control site stimulation suggests that stimulation at the control site did have a neurophysiological, if not behavioural, effect, perhaps explained by the less well-focused pressure field for the deeper target (Supplementary Table 1; Supplementary Fig. 2). However, no significant difference was detected when we compared ERPs from control site and sham stimulation trials (Supplementary Fig. 7).

Finally, we investigated whether there was any relationship between the behavioural and electrophysiological effects. The correlation coefficient between stimulation induced changes in ERP

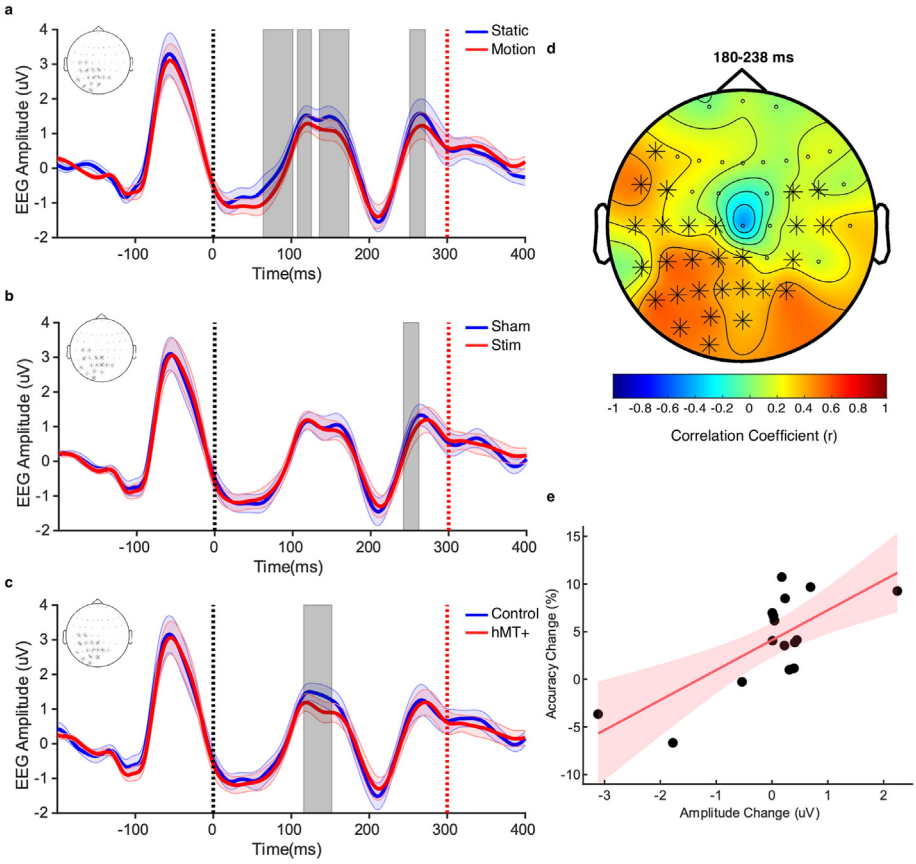


Fig. 3. | EEG results Cluster-based permutation analysis of an initial pilot dataset revealed a significant decrease in ERP amplitude during motion trials compared to static trials in the left occipito-parietal region ($p < 0.025$). These channels can be seen in the insets of panels a, b and c. The vertical lines (0 ms, black dashed; 300 ms, red dashed) represent the onset and offset of both the visual stimuli and ultrasound. **a,** Averaged ERPs as recorded from the identified motion-specific channel cluster (inset) time-locked to stimulus onset. Static trials (blue) were compared with motion trials (red), significant differences represented by grey rectangles ($p < 0.025$). **b,** Averaged ERPs as recorded from the identified motion-specific cluster (inset) time-locked to stimulus onset. Sham trials (blue) were compared with hMT+ stimulation trials (red), significant differences represented by the grey rectangle ($p < 0.025$). **c,** Averaged ERPs as recorded from the identified motion-specific cluster (inset) time-locked to stimulus onset. Control site stimulation trials (blue) were compared with hMT+ stimulation trials (red), significant differences represented by the grey rectangle ($p < 0.025$). **d,** Permutation analysis was performed to identify time-points at which stimulation-induced changes in amplitude significantly correlated with hMT+ stimulation-induced changes in accuracy performance. Significant time-points are represented by the red rectangle ($p < 0.025$). **e,** Linear regression revealed a significant relationship between average amplitude change in the identified channel cluster and accuracy change ($r^2 = 0.484$, $p = 0.003$), though note that this relationship may be driven by a few subjects (see text). (For interpretation of the references to colour in this figure legend, the reader is referred to the Web version of this article.)

amplitude in the identified cluster and the change in accuracy due to hMT+ stimulation was calculated for the same time window of stimulus presentation (0–300 ms). Permutation of these correlation values revealed a significant positive relationship between stimulation induced amplitude and accuracy change (Fig. 3d and e), in a time window 186–230 ms ($r = 0.620$, $p = 0.005$). Furthermore, linear regression of the mean amplitude change within the identified time window and the accuracy change revealed this amplitude difference accounted for 48.4% of the variance in accuracy change ($F(1,14) = 13.120$, $p = 0.003$, $r2 = 0.484$). This time window coincides with the well-recognised N2 ERP component to visual motion, which is thought to arise from hMT+ [46] and the amplitude of which has been shown to correlate with motion coherence and behavioural performance [47]. Whilst this correlation is strongly statistically significant, visual inspection suggests that it is driven by a subset of individuals in whom, in contrast to the other participants, there was a reduction in N2 amplitude with TUS and a decrease in accuracy on the task. This interesting result deserves further attention in future studies.

No side effects of stimulation were reported by any participant. Examination of T1-weighted, T2-weighted and susceptibility weighted imaging (SWI) MRI scans by an experienced Consultant Neuroradiologist (FS) revealed no difference in pre- and post-stimulation images for any of the 13 scanned participants (Supplementary Fig. 8).

4. Discussion

We demonstrate for the first time that higher order cognitive function in humans can be modulated in an anatomically precise manner by TUS. 500 kHz ultrasound, delivered transcranially to hMT+ via a single-element focused transducer, improved the accuracy and reduced the response time of visual motion discrimination. Moreover, TUS modulated the visual motion specific ERP, and the magnitude of this physiological effect correlated with the behavioural response across individuals. These results pave the way for TUS to be exploited for the fine-grained investigation of causal brain-behaviour relations in humans.

Importantly, the behavioural and EEG effects of TUS were seen in the absence of any detectable auditory confound. Recent work has raised concern that previous results in both animals and humans may have been biased by an auditory signal at the PRF transmitted through the skull to the cochlear [17–20]. The audio mask that we delivered via earphones prevented participants from

accurately discriminating stimulation from sham trials, or stimulation of hMT+ from the control site. Moreover, there was no evidence that the behavioural change caused by TUS correlated across participants with their performance on the stimulation detection task. Further evidence against the presence of an auditory confound in our experiment comes from the absence of any behavioural effect of TUS to the control site and of any EEG difference between control site stimulation and sham trials. Our results therefore provide confidence that the behavioural and EEG effects of TUS are indeed driven directly by ultrasonic neural stimulation at the target brain region.

Our finding of behavioural facilitation is in line with previous human studies of TUS to primary somatosensory cortex [6,8]. We observed improved accuracy with TUS to hMT+ and that TUS led to faster response times for accurate trials only, whilst inaccurate responses became slower. We interpret these results as supportive of the view that TUS to hMT+ modulates task-specific (i.e. visual motion) rather than non-specific (e.g. motor speed) processes, which might be expected to modulate accurate and inaccurate trials in the same direction. As with other brain stimulation methods, the directionality of behavioural effects with TUS likely depends upon the stimulation parameters used as well as the task and brain regions involved [12,48]. Based upon pilot data and the desire to remain within our prespecified safety limits for temperature and time averaged intensity, we intentionally restricted the range of difficulty (proportion of coherent motion) across trials. This lack of variability in stimulus strength precluded detailed exploration of the cognitive mechanisms underpinning the effect of TUS on visual motion detection, such as would be possible by, for example, fitting drift decision models [49]. These mechanisms should be addressed by future work.

The EEG recording and analysis in this experiment were complicated by two factors. First, we had to remove electrodes in order to allow room for the TUS transducer. The transducer was placed directly above hMT+ in the right hemisphere, the region where EEG effects might be expected to be maximal. To work around this, we first used data from a pilot study to identify which existing channels showed a visual motion specific ERP and focused our investigation of TUS effects on this cluster. Our observation that TUS modulated the visual motion specific ERP in contralateral posterior channels is consistent with the bilateral representation of visual motion in the brain and with the bihemifield effects of unilateral TMS to hMT+ [43]. Second, the audio mask induced a large positive ERP before stimulus presentation, which may have attenuated the detectability of TUS-related EEG changes. This is clearly better than not controlling for the auditory confound at all but alternative approaches, such as using continuous wave ultrasound and ramping the onset and offset of the pulse, could be explored as a means of removing auditory stimulation completely. The correlation we observed between the behavioural and electrophysiological effects of TUS across individuals suggests that the neural changes induced by TUS in hMT+ directly underpin the modulation in behavioural performance. Such causal relationships could be further explored in future studies by varying the acoustic intensity at the target in a controlled way within participants and testing for correlated behavioural and EEG modulation.

In order to focus ultrasound to the desired target location in the brain we employed participant-specific modelling. The skull geometry for each participant was obtained from MR imaging since CT was not considered justifiable in healthy volunteers. MR has limitations in accuracy for determining the surface and internal structure of the skull. We did carry out a sensitivity analysis of our computer simulations (varying all the material properties) and, for the 500 kHz frequency and target locations employed in this study, the pressure amplitude predictions were affected by less than 10%. In future, it would be helpful to improve the determination of skull morphology, for example by using newer MR methods such as ultrashort TE sequences [50], as well as improving the ultrasound material properties for bone, in particular sound speed and attenuation, in order to make the predictions of the pressure field more accurate.

Our findings provide, for the first time and with a rigorously controlled experimental paradigm, behavioural and correlating electrophysiological evidence that TUS can be safely used to modulate higher-order cognitive processing in humans. TUS to hMT+ improved the accuracy and accurate response time of visual motion detection. The effect of TUS was anatomically specific and correlated with the EEG response to stimulation.

Data availability

Data are publicly available at osf.io/j5wdu.

CRediT authorship contribution statement

Christopher R. Butler: conceived and planned the experiments, carried out the experiments, carried out data analysis and contributed to the interpretation of the results, Data curation, Formal analysis, wrote the manuscript with contribution from all authors. **Edward Rhodes:** carried out data analysis and contributed to the interpretation of the results, Data curation, Formal analysis. **Joseph Blackmore:** conceived and planned the experiments, carried out the experiments, carried out data analysis and contributed to the interpretation of the results, Data curation, Formal analysis. **Xinghao Cheng:** carried out data analysis and contributed to the interpretation of the results, Data curation, Formal analysis. **Robert L. Peach:** carried out data analysis and contributed to the interpretation of the results, Data curation, Formal analysis. **Michele Veldsman:** conceived and planned the experiments. **Fintan Sheerin:** carried out data analysis and contributed to the interpretation of the results, Data curation, Formal analysis. **Robin O. Cleveland:** conceived and planned the experiments, carried out the experiments, carried out data analysis and contributed to the interpretation of the results, Data curation, Formal analysis.

Declaration of competing interest

The authors declare that they have no known competing financial interests or personal relationships that could have appeared to influence the work reported in this paper.

Acknowledgements

We thank Dr Verena Braun for contributing to the smooth running of the trial. This work was supported by the Oxford University John Fell Foundation and the Engineering and Physical Sciences Research Council (EPSRC; Grant No. EP/F500394/1). We also gratefully acknowledge the support of NVIDIA Corporation with the donation of the Titan Xp GPU used for this research.

Appendix A. Supplementary data

Supplementary data to this article can be found online at https://doi.org/10.1016/j.brs.2022.08.022.

References

[1] Rabut C, et al. Ultrasound technologies for imaging and modulating neural activity. Neuron 2020;108:93–110.

[2] Tufail Y, et al. Transcranial pulsed ultrasound stimulates intact brain circuits. Neuron 2010;66:681–94.
[3] Folloni D, et al. Manipulation of subcortical and deep cortical activity in the primate brain using transcranial focused ultrasound stimulation. Neuron 2019;101:1109–16. e5.
[4] Lee W, et al. Image-guided focused ultrasound-mediated regional brain stimulation in sheep. Ultrasound Med Biol 2016;42:459–70.
[5] Fouragnan EF, et al. The macaque anterior cingulate cortex translates counterfactual choice value into actual behavioral change. Nat Neurosci 2019;22:797–808.
[6] Legon W, et al. Transcranial focused ultrasound modulates the activity of primary somatosensory cortex in humans. Nat Neurosci 2014;17:322–9.
[7] Lee W, et al. Image-guided transcranial focused ultrasound stimulates human primary somatosensory cortex. Sci Rep 2015;5:8743.
[8] Liu C, Yu K, Niu X, He B. Transcranial focused ultrasound enhances sensory discrimination capability through somatosensory cortical excitation. Ultrasound Med Biol 2021;47:1356–66.
[9] Lee W, et al. Transcranial focused ultrasound stimulation of human primary visual cortex. Sci Rep 2016;6:34026.
[10] Legon W, Bansal P, Tyshynsky R, Ai L, Mueller JK. Transcranial focused ultrasound neuromodulation of the human primary motor cortex. Sci Rep 2018;8:10007.
[11] Ai L, Bansal P, Mueller JK, Legon W. Effects of transcranial focused ultrasound on human primary motor cortex using 7T fMRI: a pilot study. BMC Neurosci 2018;19:10–56.
[12] Fomenko A, et al. Systematic examination of low-intensity ultrasound parameters on human motor cortex excitability and behaviour. Elife 2020;9:1–68.
[13] Yu K, Liu C, Niu X, He B. Transcranial focused ultrasound neuromodulation of voluntary movement-related cortical activity in humans. IEEE Trans Biomed Eng 2021;68:1923–31.
[14] Xia X, et al. Time course of the effects of low-intensity transcranial ultrasound on the excitability of ipsilateral and contralateral human primary motor cortex. Neuroimage 2021;243:118557.
[15] Legon W, Ai L, Bansal P, Mueller JK. Neuromodulation with single-element transcranial focused ultrasound in human thalamus. Hum Brain Mapp 2018;39:1995–2006.
[16] Badran BW, et al. Sonication of the anterior thalamus with MRI-Guided transcranial focused ultrasound (tFUS) alters pain thresholds in healthy adults: a double-blind, sham-controlled study. Brain Stimul 2020;13:1805–12.
[17] Guo H, et al. Ultrasound produces extensive brain activation via a cochlear pathway. Neuron 2018;98:1020–30. e4.
[18] Sato T, Shapiro MG, Tsao DY. Ultrasonic neuromodulation causes widespread cortical activation via an indirect auditory mechanism. Neuron 2018;98:1031–41. e5.
[19] Braun V, Blackmore J, Cleveland RO, Butler CR. Transcranial ultrasound stimulation in humans is associated with an auditory confound that can be effectively masked. Brain Stimul 2020;13:1527–34.
[20] Johnstone A, et al. A range of pulses commonly used for human transcranial ultrasound stimulation are clearly audible. Brain Stimul 2021;14:1353–5.
[21] Salahshoor H, Shapiro MG, Ortiz M. Transcranial focused ultrasound generates skull-conducted shear waves: computational model and implications for neuromodulation. Appl Phys Lett 2020;117.
[22] Blackmore J, Shrivastava S, Sallet J, Butler CR, Cleveland RO. Ultrasound neuromodulation: a review of results, mechanisms and safety. Ultrasound Med Biol 2019;45:1509–36.
[23] Zeki S. Area V5-a microcosm of the visual brain. Front Integr Neurosci 2015;9:21.
[24] Kanwisher N, McDermott J, Chun M. The fusiform face area: a module in human extrastriate cortex specialized for face perception. J Neurosci 1997;17:4302–11.
[25] Tootell RBH, et al. Functional analysis of human MT and related visual cortical areas using magnetic resonance imaging, 15; 1995.
[26] Berman MG, et al. Evaluating functional localizers : the case of the FFA. Neuroimage 2011;50:56–71.
[27] Treeby BE, Cox B T k-Wave. MATLAB toolbox for the simulation and reconstruction of photoacoustic wave fields. J Biomed Opt 2010;15:021314.
[28] Treeby BE, Cox BT. Modeling power law absorption and dispersion for acoustic propagation using the fractional Laplacian. J Acoust Soc Am 2010;127:2741–8.
[29] Blackmore J. Focused ultrasound: a non-invasive brain stimulation modality. University of Oxford; 2018.
[30] Hasgall, P. A. et al. IT'IS Database for thermal and electromagnetic parameters of biological tissues, Version 4.0. https://itis.swiss/virtual-population/tissue-properties/doi:10.13099/VIP21000-04-0.
[31] Duck FA. Medical and non-medical protection standards for ultrasound and infrasound. Prog Biophys Mol Biol 2007:93 176–191.
[32] Constans C, Mateo P, Tanter M, Aubry JF. Potential impact of thermal effects during ultrasonic neurostimulation: retrospective numerical estimation of temperature elevation in seven rodent setups. Phys Med Biol 2018;63.
[33] Treeby BE, Cox BT. Modeling power law absorption and dispersion in viscoelastic solids using a split-field and the fractional Laplacian. J Acoust Soc Am 2014;136:1499–510.
[34] Mueller JK, Ai L, Bansal P, Legon W. Numerical evaluation of the skull for human neuromodulation with transcranial focused ultrasound. J Neural Eng 2017;14.
[35] Top CB, White PJ, McDannold NJ. Nonthermal ablation of deep brain targets: a simulation study on a large animal model. Med Phys 2016;43:870–82.
[36] Sapozhnikov OA, Tsysar SA, Khokhlova VA, Kreider W. Acoustic holography as a metrological tool for characterizing medical ultrasound sources and fields. J Acoust Soc Am 2015;138:1515–32.
[37] Pennes HH. Analysis of tissue and arterial blood temperatures in the resting human forearm. J Appl Physiol 1948;1:93–122.
[38] Nyborg WL. Heat generation by ultrasound in a relaxing medium. J Acoust Soc Am 1981;70:310–2.
[39] Eames M, Hananel A, Snell JW, Kassell NF, Aubry J-F. Trans-cranial focused ultrasound without hair shaving: feasibility study in an ex vivo cadaver model. 2013. http://www.jtultrasound.com/content/1/1/24.
[40] Watson AB, Pelli DG. QUEST: a Bayesian adaptive psychometric method. Percept Psychophys 1983;33:113–20.
[41] Oostenveld R, Fries P, Maris E, Schoffelen J-M. FieldTrip: open source software for advanced analysis of MEG, EEG, and invasive electrophysiological data. Comput Intell Neurosci 2011;2011:156869.
[42] Zaksas D, Pasternak T. Area MT neurons respond to visual motion distant from their receptive fields. J Neurophysiol 2005;94:4156–67.
[43] Strong SL, Silson EH, Gouws AD, Morland AB, McKeefry DJ. An enhanced role for right hV5/MT+ in the analysis of motion in the contra- and ipsi-lateral visual hemi-fields. Behav Brain Res 2019;372:112060.
[44] Bolsinova M, Tijmstra J, Molenaar D, De Boeck P. Conditional dependence between response time and accuracy: an overview of its possible sources and directions for distinguishing between them. Front Psychol 2017;202. https://doi.org/10.3389/FPSYG.2017.00202.
[45] Kuba M, Kubová Z, Kremláček J, Langrová J. Motion-onset VEPs: characteristics, methods, and diagnostic use. Vis Res 2007;47:189–202.
[46] Aspell JE, Tanskanen T, Hurlbert AC. Neuromagnetic correlates of visual motion coherence. Eur J Neurosci 2005;22:2937–45.
[47] Patzwahl DR, Zanker JM. Mechanisms of human motion perception: combining evidence from evoked potentials, behavioural performance and computational modelling. Eur J Neurosci 2000;12:273–82.
[48] Yoon K, et al. Effects of sonication parameters on transcranial focused ultrasound brain stimulation in an ovine model. PLoS One 2019;14:e0224311.
[49] Ratcliff R, Smith PL, Brown SD, McKoon G. Diffusion decision model: current issues and history. Trends Cognit Sci 2016;20:260–81.
[50] Johnson, E. M., Vyas, U., Ghanouni, P., Butts Pauly, K. & Pauly, J. M. Improved cortical bone specificity in UTE MR imaging. doi:10.1002/mrm.26160.